SUPERCELL THUNDERSTORM UPDRAFT ACCELERATIONS DURING THE EVENING TRANSITION

A Thesis

by

MARC BREMENKAMP

Submitted to the Graduate and Professional School of
Texas A&M University
in partial fulfillment of the requirements for the degree of

MASTER OF SCIENCE

Chair of Committee,	Christopher J. Nowotarski
Committee Members,	Craig Epifanio
	Robert Hetland
Head of Department,	R. Saravanan

August 2021

Major Subject: Atmospheric Sciences

ABSTRACT

The evolution of supercell thunderstorm environments during the evening transition provides mechanisms that would seemingly offer competing contributions to updraft accelerations: low-level cooling and associated stabilization detrimental to buoyancy accelerations and a low-level jet favorable to dynamic accelerations. To determine the impacts of changes to the thermodynamic and kinematic profiles on updraft accelerations during the evening transition, a suite of idealized simulations is initialized with unique combinations of thermodynamic and kinematic profiles representative of various stages of the evening transition. The core updraft is defined at each height for each simulation, and profiles of average acceleration terms within the updraft core are compared amongst simulations. It was found that the relative contributions of dynamic accelerations increased early in the evening transition but were not sustained. The thermodynamic evolution of the evening transition weakens low-level net updraft accelerations. The kinematic profile evolution increases low-level net updraft accelerations early in the evening transition, but those gains are lost later in the evening transition. Near-ground vertical vorticity stretching, an important mechanism in tornadogenesis, is most favored by the mid-transition kinematic profile.

ACKNOWLEDGEMENTS

I would like to thank my committee chair, Dr. Nowotarski, and my committee members, Dr. Epifanio and Dr. Hetland, for their guidance and support during this research.

Thanks also go to my friends and colleagues and the department of Atmospheric Sciences faculty and staff for their support and for making my time at Texas A&M University a great experience.

Thanks go to my parents and siblings for their support and for helping to provide the opportunities to pursue my intellectual curiosities.

Finally, thanks go to my wife, Caitlyn, for her patience, love, and support through my time at Texas A&M and particularly through the Covid-19 pandemic.

CONTRIBUTORS AND FUNDING SOURCES

Contributors

This work was supervised by a thesis committee consisting of Dr. Christopher Nowotarski and Dr. Craig Epifanio of the Department of Atmospheric Sciences and Dr. Robert Hetland of the Department of Oceanography.

We would like to acknowledge high-performance computing support from Cheyenne (*doi:10.5065/D6RX99HX*) provided by NCAR's Computational and Information Systems Laboratory, sponsored by the National Science Foundation.

All work conducted for the thesis was completed by the student independently.

Funding Sources

This work was supported by National Science Foundation grant: AGS-1928319. Its contents are solely the responsibility of the authors and do not necessarily represent the official views of the National Science Foundation.

NOMENCLATURE

BP	Buoyancy pressure acceleration
BUOY	Buoyancy acceleration
CAPE	Convective available potential energy
CIN	Convective inhibition
CM1	Cloud Model 1
CPBL	Convective planetary boundary layer simulation
DYN	Dynamic acceleration
ET	Evening transition
LCL	Lifted condensation level
LFC	Level of free convection
LLJ	Low-level jet
MU	Most unstable
NET	Net acceleration
q_v	Water vapor mixing ratio
SB	Surface based
SRH	Storm-relative helicity
TW	Updraft core threshold vertical velocity
T0	Pre-transition thermodynamic profile
T1	Mid-transition thermodynamic profile
T2	Post-transition thermodynamic profile
VPPGF	Vertical perturbation pressure gradient force

VVS	Vertical vorticity stretching
w	Vertical velocity
W0	Pre-transition kinematic profile
W1	Mid-transition kinematic profile
W2	Post-transition kinematic profile
ρ_0	Base-state density
θ	Potential temperature
ζ	Vertical vorticity

TABLE OF CONTENTS

LIST OF FIGURES

LIST OF TABLES

Page

1. INTRODUCTION

1.1. Background

Supercell thunderstorms are an important focus of scientific inquiry due to their capacity to produce life-threatening, socioeconomic hazards and their physical complexity. Supercells are distinguished from other thunderstorms by their steady, large, intense, and rotating updraft, known as the mesocyclone, and can produce hazards such as lightning, flash flooding, hail, and tornadoes. Indeed, most tornadoes are associated with supercells (Smith et al., 2012). Additionally, nocturnal tornadoes result in a disproportionate fraction of tornado fatalities (Ashley et al., 2008). Tornadogenesis requires stretching of vertical vorticity by low-level vertical accelerations (Markowski and Richardson, 2014; Coffer and Parker, 2015). Therefore, it is important to study supercell thunderstorms and their updraft accelerations in evening and nocturnal environments.

The evening transition (ET), sometimes referred to as the nocturnal transition, is characterized by thermodynamic and kinematic changes in the lowest levels of the atmosphere immediately preceding and following sunset. During this period, the loss of solar insolation leads to radiative cooling of Earth's surface, which in turn results in cooling of the near-surface atmosphere and the formation of a temperature inversion and stable layer (Stull, 1988). Evapotranspiration continues to occur at the surface after sunset, and the near-surface stable layer moistens (Blumberg et al., 2019). Additionally, when the near-surface stable layer forms, convective mixing within the layer ceases.

Thus, the effects of surface friction are removed above the stable layer, causing an acceleration and formation of a low-level jet (LLJ; Shapiro et al., 2016).

Amongst the modes of atmospheric convection, supercell thunderstorms can produce the strongest observed vertical velocity (Lehmiller et al., 2001). There are three primary acceleration terms that contribute to supercell updraft velocity:

$$\frac{dw}{dt} = BUOY - \frac{1}{\rho_0}\frac{\partial p_b'}{\partial z} - \frac{1}{\rho_0}\frac{\partial p_d'}{\partial z}.$$

The first term on the right-hand side is buoyancy, the second term is the nonhydrostatic vertical perturbation pressure gradient force (VPPGF) due to buoyancy, and the third term is nonhydrostatic VPPGF due to dynamic effects. Buoyancy accelerations are created by differences between a parcel's density and the density of its environment. Buoyancy pressure accelerations arise from VPPGFs across a parcel and generally act in the opposite direction of buoyancy accelerations. The dynamic pressure perturbation and the associated vertical acceleration can be broken down into two components: nonlinear and linear. Nonlinear dynamic pressure perturbations consist of 'spin' and 'splat' terms which are associated with vorticity and deformation, respectively. Linear dynamic pressure perturbations arise from wind shear interacting with storm updrafts (Markowski and Richardson, 2010; Peters et al., 2019).

During the ET, increased low-level wind shear associated with the LLJ can act to increase storm-relative helicity (SRH; Gropp and Davenport, 2018). Increased SRH has been shown in previous studies to increase low-level dynamic accelerations, particularly at low levels of the updraft and enhance updraft velocity (Coffer and Parker, 2015; Peters et al., 2019). The enhancement of low-level dynamic accelerations through increased SRH also has been shown to help supercells maintain updraft velocity, although weaker, in cases of increased near-surface thermodynamic stability (Nowotarski et al., 2011; Coffer and Parker, 2015; Gropp and Davenport, 2018). Storm-relative inflow, which may increase with LLJ onset, also has been shown to be important to updraft velocity. Greater storm-relative inflow leads to wider updrafts such that the cores of wider updrafts are less diluted by entrainment (Peters et al., 2019). However, previous literature has largely neglected the impacts of ET thermodynamic and kinematic changes on individual updraft acceleration terms and the evolution of the relative contributions of those terms.

The goal of this study is to identify the separate impacts of ET thermodynamic and kinematic changes on supercell updraft accelerations and velocity using idealized simulations. The thermodynamic and kinematic changes characteristic of the ET would seemingly present competing contributions to updraft accelerations. On one hand, the near-surface atmospheric cooling acts to reduce the convective available potential energy (CAPE) available to the storm and increases the convective inhibition (CIN) of the environment. These changes are generally detrimental to buoyant accelerations within the storm. On the other hand, near-surface moistening will act to increase CAPE and decrease CIN, although the effects of cooling are typically dominant. Additionally, the introduction of a LLJ may act to increase SRH, which can act to increase dynamic updraft accelerations, particularly at low levels (Coffer and Parker, 2015; Gropp and Davenport, 2018). The LLJ may also widen updrafts through increased low-level storm inflow, resulting in stronger mid-level updrafts as entrainment decreases, despite decreases in CAPE. Due to the competing nature of the expected effects of the ET on supercell updraft accelerations, a method capable of isolating the individual effects through controlled experiments is necessary. Therefore, a suite of idealized numerical simulations was chosen to investigate the research questions and accompanying hypotheses in the following section.

1.2. Research Questions and Hypotheses

1.2.1. During the ET, how do the relative contributions of buoyant and dynamic updraft accelerations change? How is updraft velocity in turn affected?

It is expected that the relative contribution of dynamic accelerations and updraft velocity will increase at low levels, but that mid-level and peak updraft velocity will generally decrease through the ET.

1.2.2. How do thermodynamic and kinematic changes of the ET individually affect updraft accelerations and velocity?

It is expected that thermodynamic changes during the ET will decrease buoyant updraft accelerations, and it is expected that kinematic changes during the ET will increase dynamic updraft accelerations, particularly at low levels.

1.2.3. Do any environmental changes during the ET affect near-surface vertical vorticity stretching?

It is expected that increased low-level dynamic accelerations caused by kinematic changes during the ET will increase near-surface vertical vorticity stretching.

2. METHODS

2.1. Model Setup and Initialization

All simulations within this study were run with Cloud Model 1 (CM1) version 20.1 (Bryan and Fritsch 2002). CM1 is a non-hydrostatic, compressible, time-dependent, three-dimensional model used in idealized studies of atmospheric phenomena such as tropical cyclones, squall lines, and supercell thunderstorms (Bryan and Fritsch, 2002). The horizontal grid spacing in both x and y directions was set to 250 m. There were 480 grid points in both horizontal directions for a domain size of 120 km x 120 km. The vertical grid spacing was set to 50 m in the lowest three kilometers and stretched to 500 m above eight kilometers. The total domain height was 18 km and consisted of 99 vertical levels. The lower and upper boundaries were set as “free-slip.” Rayleigh damping was applied above 15 km to dampen vertically propagating waves. The lateral boundary conditions were set as “open-radiative” (Durran and Klemp, 1983). All the simulations were run for a duration of three hours with a large time step of one second. Simulation data were output every 10 minutes. The microphysics processes were represented by the double-moment scheme of Morrison et al. (2009). The simulations did not include Coriolis force, radiation physics, or surfaces fluxes of heat, moisture, and momentum.

Convection within each simulation was initialized using the updraft nudging technique of Naylor and Gilmore (2012). The maximum updraft nudging amplitude was 10 m s^{-1} and was located at the horizontal center of the domain at a height of 1.5 km. The vertical radius of the nudging was 1.5 km, and the horizontal radius of the nudging was

10 km. The updraft nudging lasted for a total of 20 minutes. The updraft nudging operated at the full amplitude over the first 15 minutes before weakening over the next five minutes. Besides the updraft nudging, the domain environment was horizontally homogeneous to begin each simulation. The distinguishing features between the simulations are the base-state thermodynamic and kinematic vertical profiles, which are described in the following sections.

2.2. Model Environments

To isolate the effects of the ET on mature supercell thunderstorms, a unique combination of thermodynamic and kinematic profiles was used for each simulation. For both thermodynamic and kinematic profiles, three characteristic profiles were created: pre-transition, mid-transition, and post-transition. With three thermodynamic and three kinematic profiles, a total of nine unique environments were used to initialize the nine simulations within this study.

2.2.1. Thermodynamic Profiles

Three thermodynamic profiles were created to represent the cooling and moistening of the near-surface atmosphere during the nocturnal transition. Hereafter, the pre-transition, mid-transition, and post-transition thermodynamics profiles will be denoted by T0, T1, and T2, respectively. The T0 profile was obtained from previous work that simulated a convective planetary boundary layer during the late afternoon and evening transition (Bremenkamp and Nowotarski, 2020). The simulation from which T0 was obtained, denoted as CPBL, used CM1 with radiation physics, surface fluxes of heat, moisture, and momentum, and initial random 0.1 K potential temperature (θ) perturbations in the lowest one kilometer. CPBL was initialized using a modified version of the sounding from Weisman and Klemp (1982). T0 is composed of the horizontal average of θ and water vapor (q_v) at each model height level one hour before sunset during CPBL, after which the near-surface layer began to cool and moisten (Figure 2.1). Thus, T0 is considered the pre-transition profile.

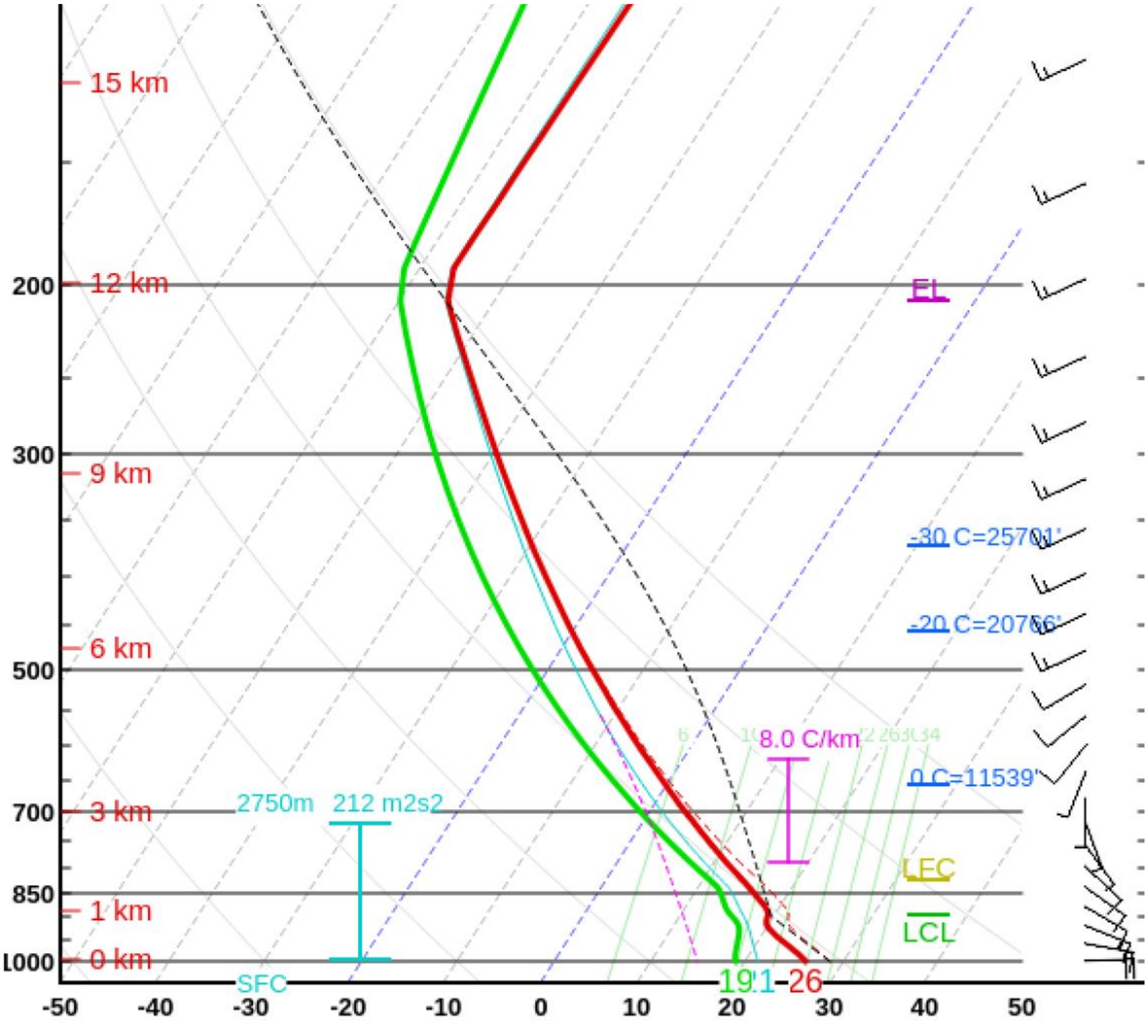

Figure 2.1 Skew-T Log-P diagram of the T0 profile featuring dewpoint temperature (green), wet-bulb temperature (blue), temperature (solid red), virtual temperature, (dashed red), and virtual temperature of lifted most unstable parcel (dashed black).

The T1 and T2 profiles were created to represent the thermodynamic profile about two and four hours after sunset, respectively, by adding perturbations to cool and moisten the lowest height levels of T0. To create the T1 profile, surface perturbations of -3 K and 0.5 g kg^{-1} were applied to T0. The perturbation magnitude decreased exponentially with height over a depth of 450 m (Figure 2.2b). Meanwhile, the T2 profile was created by applying surface perturbations of -6 K and 1.0 g kg^{-1} to T0. The perturbation magnitude decreased exponentially with height over a depth of 750 m (Figure 2.2c). The depth and rate of decay with height of the perturbations were based on the post-sunset evolution of the thermodynamic profile in CPBL. The magnitudes of the q_v perturbations were based on the post-sunset evolution of CPBL and Blumberg et al. (2019). The magnitude of the θ perturbations were chosen to maximize the surface cooling while avoiding near-surface fog formation (i. e., saturation) in the simulation that would complicate the analysis.

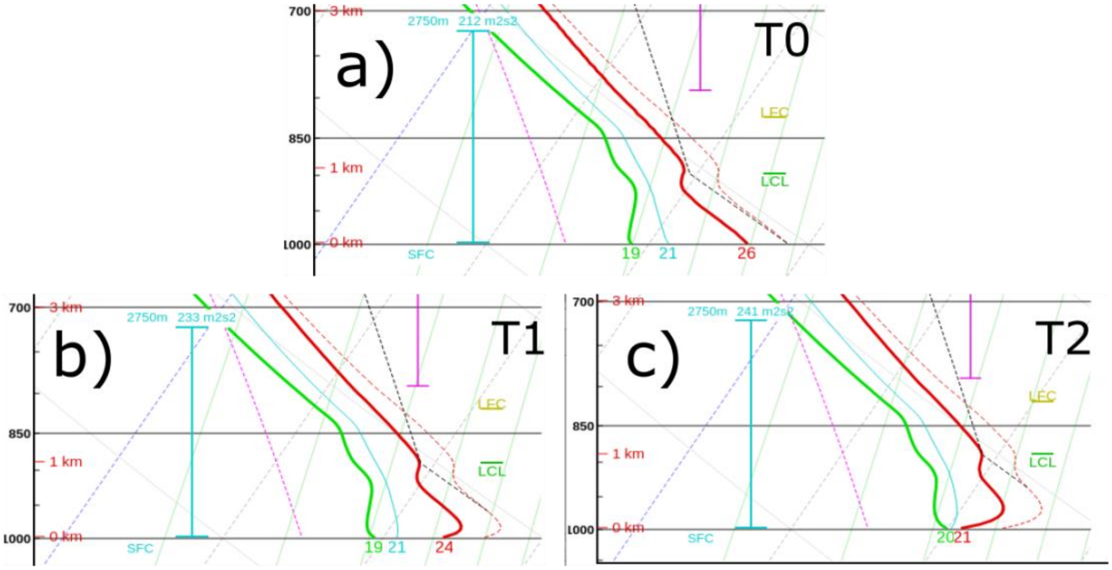

Figure 2.2 Skew-T Log-P diagrams of the lowest height levels of the thermodynamic profiles T0 (a), T1 (b), and T2 (c).

The introduction of low-level cooling and moistening in the T1 and T2 profiles resulted in changes to the convective parameters associated with the surface-based (SB) and most-unstable (MU) parcels (Table 2.1). For the SB parcel, CAPE decreases through the ET, while the magnitude of CIN increases. The lifted condensation level (LCL) of the SB parcel decreases through the ET. Meanwhile, the level of free convection (LFC) increases for the SB parcel. The changes to all the convective parameters are lesser in magnitude for the MU parcel than the SB parcel. For the MU parcel, CAPE decreases slightly, CIN is constant, LCL increases slightly through the ET. Meanwhile, the LFC of the MU parcel increases slightly from T0 to T1, then the LFC decreases by one meter from T1 to T2.

Table 2.1 Convective parameters for SB and MU parcels associated with each thermodynamic profile.

Parcel	SB			MU		
Profile	T0	T1	T2	T0	T1	T2
CAPE (J kg^{-1})	2484	2162	1763	2484	2367	2333
CIN (J kg^{-1})	-40	-105	-153	-40	-40	-40
LCL (m)	919	568	138	919	989	994
LFC (m)	1650	1802	1950	1650	1701	1700

2.2.2. Kinematic Profiles

Three kinematic profiles were created to represent the introduction and strengthening of the LLJ after sunset. Like the thermodynamic profiles, the pre-transition, mid-transition, and post-transition kinematic profiles will be denoted by W0, W1, and W2, respectively. The hodograph of the W0 profile consists of a clockwise rotating quarter-circle in the lowest kilometer, westerly shear from 1-6 km, and no shear above six kilometers (Figure 2.3a). This profile, and variations thereof, is commonly used in idealized simulations of supercell thunderstorms. The W1 and W2 profiles are intended to temporally coincide with T1 and T2, respectively, and introduce the LLJ by adding perturbations to W0 (Figure 2.3b-c). The characteristics of the LLJ perturbations were determined based on LLJ climatologies and case studies (Whiteman et al. 1997; Song et al., 2005; Smith et al., 2019). The perturbation of W1 had a maximum magnitude of five m s^{-1} and was southerly. Meanwhile the perturbation of W2 had a maximum magnitude of 10 m s^{-1} and was oriented 15 degrees west of south (Figure 2.3d).

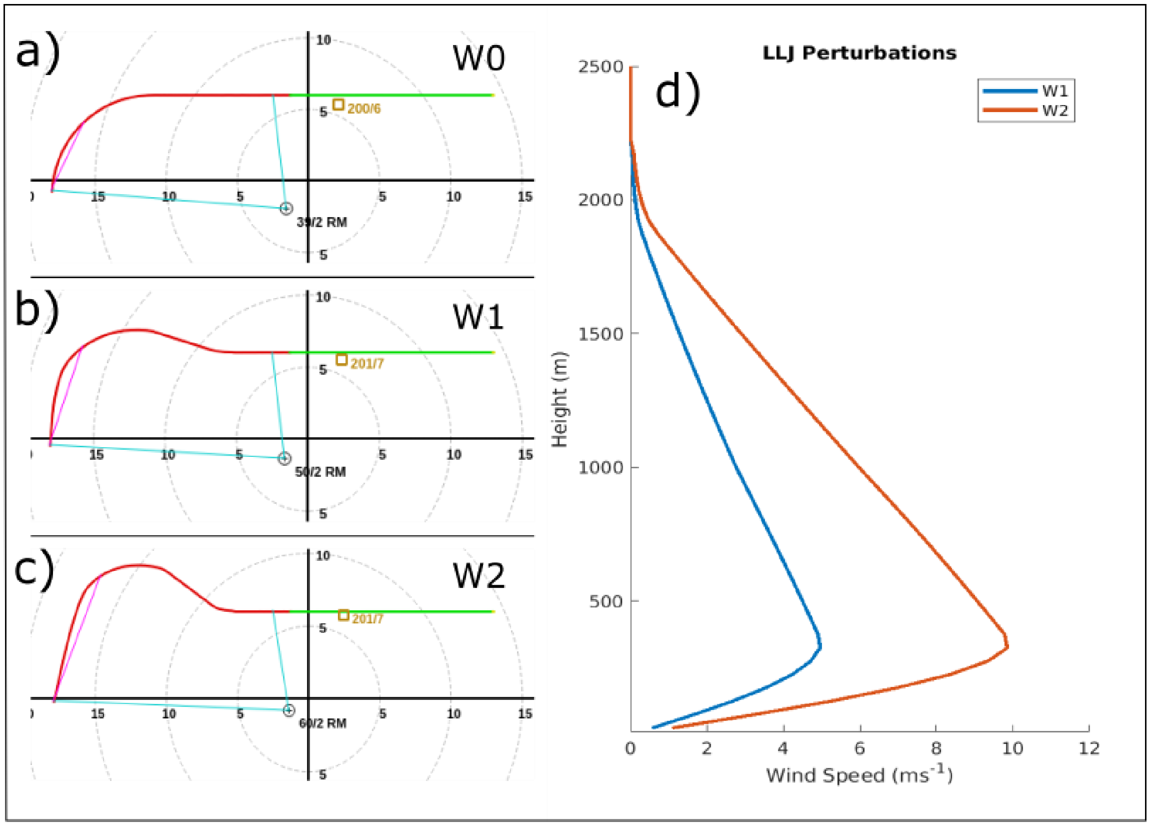

Figure 2.3 Hodographs for kinematic profiles W0 (a), W1 (b), and W2 (c) featuring winds in 0-3 km layer (red), winds in 0-6 km layer (green), winds above 6 km (yellow), 0-0.5 km wind shear (magenta), and Bunker's right storm motion (black circle). Vertical profile of wind speed perturbations applied to W1 (blue) and W2 (red) profiles (d).

By introducing LLJ perturbations to the W1 and W2 profiles, the SRH associated with the profiles increased relative to the W0 profile (Table 2.2). SRH increased through the ET for both the 0-1 km and 0-3 km layers.

Table 2.2 SRH associated with each kinematic profile from 0-1 km and 0-3 km.

Profile	W0	W1	W2
0-1 km SRH (m^2 s^{-2})	146	178	203
0–3-km SRH (m^2 s^{-2})	222	242	249

Each of the nine simulations is named based on the initial environment. For example, the simulation pairing the T0 and W0 profiles is referred to as T0W0.

3. RESULTS

All nine simulations contained convection which included a dominant right-moving supercell after one hour of simulation time. To focus the analysis on the updraft of the right-moving supercell, the right-mover was tracked using the 2-5 km integrated updraft helicity. Then, a 'storm-domain' was defined as the region +/- 20 km in both x and y directions from the location of the right-mover's maximum 2-5 km integrated updraft helicity for all model times included in the analysis. Next, at each height level the 'updraft core' at that height was defined as grid points with vertical velocity (w) exceeding the 95th percentile of points with appreciable upward motion ($w > 0.1$ m s^{-1}) at that height within the storm domain. Examples of the updraft core at 100 m and 5163 m from the T1W0 simulation are shown in Figure 3.1. To focus the analysis on the mature storm stage, the simulation time range of 100 to 140 minutes was selected as representative of mature updrafts in all simulations. In the following sections, any variable represented by a vertical profile was averaged across updraft core points at each height level during the mature storm time range.

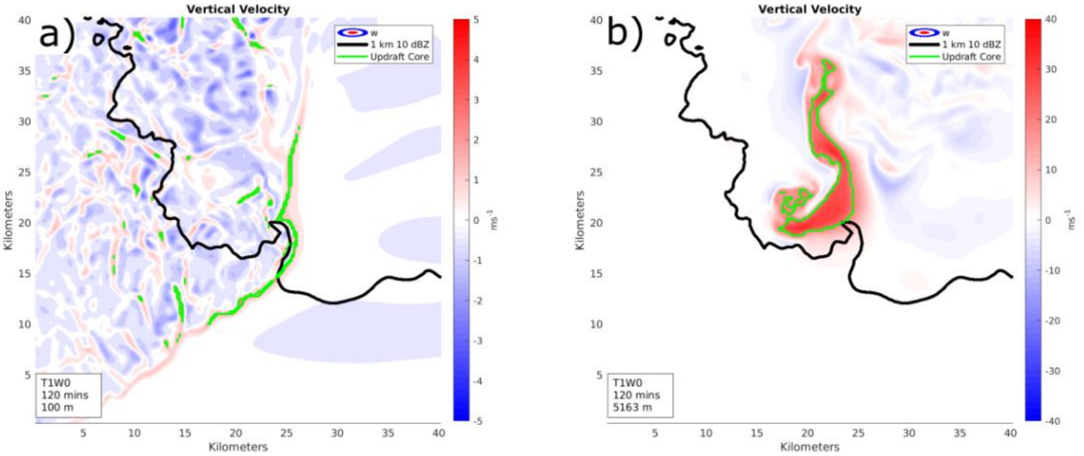

Figure 3.1 Plan view of vertical velocity contours (shaded) within the storm domain at t = 120 min in the T1W0 simulation at z = 100 m (a) and z = 5163 m (b). The simulated radar reflectivity contour of 10 dBZ at z = 1 km is overlaid in black, and the updraft core contour is overlaid in green.

3.1. Relative contributions of buoyant and dynamic accelerations during the ET.

To test the first hypothesis, three simulations were chosen: T0W0, T1W1, and T2W2 (Figure 3.2). This group of model environments most closely represents the natural ET because the thermodynamic and kinematic profiles from similar stages of the ET are paired. To determine how the relative contribution of dynamic and buoyant accelerations change during the ET, first the evolution of each acceleration term during the ET will be analyzed.

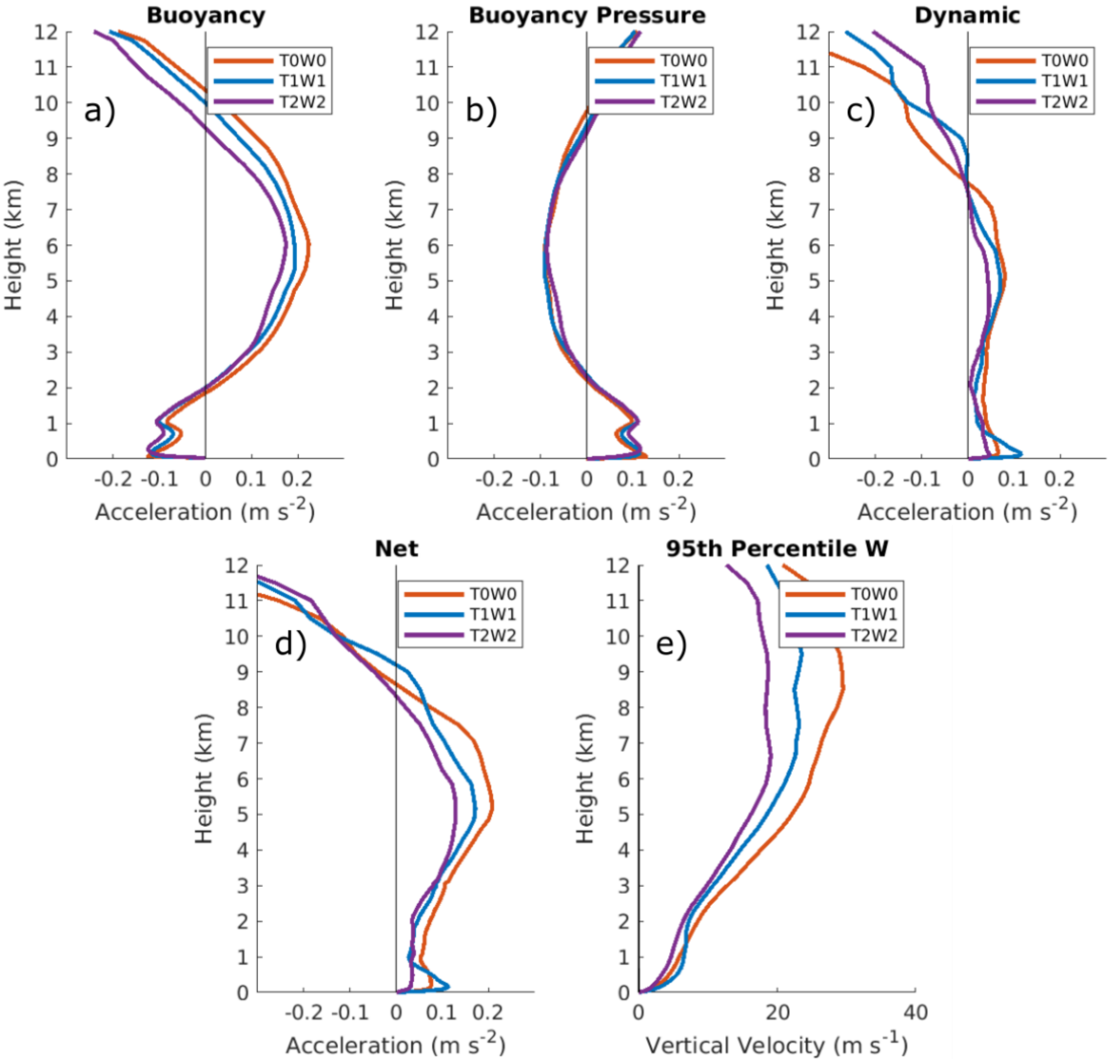

Figure 3.2 Vertical profiles of updraft core buoyancy acceleration (a), buoyancy pressure acceleration (b), dynamic acceleration (c), net acceleration (d), and updraft core threshold vertical velocity (e) featuring T0W0 (red), T1W1 (blue), and T2W2 (purple) simulations.

Figure 3.2a shows the profiles of buoyancy acceleration (BUOY). At all heights, BUOY decreases as the ET progresses (i.e., from T0W0 to T1W1 to T2W2). Buoyancy pressure acceleration (BP) increases through the ET in the lowest 1 km (Figure 3.2b). However, BP is mostly unchanged between 1 km and 8 km. Figure 3.2c shows the dynamic acceleration (DYN) profiles. The dynamic acceleration consists of the sum of nonlinear and linear dynamic accelerations. Because the linear term is often symmetric about the updraft, it is often small when averaged over the updraft core such that DYN is dominated by nonlinear dynamic pressure perturbations (Figure A.1). Below 1 km, DYN increases early in the ET before decreasing to values less than the pre-transition. DYN generally decreases through the ET between 1 km and 8 km. The net acceleration (NET) was calculated by taking the sum of BP, BUOY, and DYN at each height level (Figure 3.2d). Below 8 kilometers, NET generally decreases as the ET progresses except below 1 km, where T1W1 is the greatest due to its larger DYN. The updraft core threshold w (TW) shows a similar trend to the net acceleration (Figure 3.2e). Above 1 km, TW decreases through the ET. However below 1 km, TW is maximized in T1W1.

In the lowest height levels, the relative contributions of DYN increase early in the ET. Comparing T0W0 and T1W1 below 1 km, the differences in BUOY and BP partially offset each other, while DYN is greater in T1W1. The relative contribution of DYN is also larger earlier in the ET between 4 km and 6 km. In this layer, BP and DYN for the T0W0 and T1W1 simulations are mostly unchanged. Meanwhile, BUOY decreases from T0W0 to T1W1. Otherwise, the relative contribution of DYN remains the same or decreases at other heights early in the ET and at all heights late in the ET. Therefore, the hypothesis that the relative contribution of DYN and updraft velocity would increase in the lowest height levels was supported early in the ET, but this hypothesis is not supported late in the ET. The hypothesis that mid-level and peak updraft velocity would decrease through the ET is supported.

3.2. Isolated effects of thermodynamic and kinematic changes during the ET on updraft accelerations and velocity.

In the previous section, both the thermodynamic and kinematic profiles varied amongst the selected simulations. While that group of simulations most closely represents the natural ET, to test the second hypothesis, it is necessary to hold either the thermodynamic or kinematic profile constant within each group of simulations. Therefore, the effects on each updraft acceleration term of the variable profile within each group can be analyzed.

3.2.1. Buoyancy acceleration

3.2.1.1. Thermodynamic effects on buoyancy acceleration

To investigate the effects of the thermodynamic evolution during the ET, simulations were grouped by a common kinematic profile (Figure 3.3). It is expected that BUOY will decrease as the thermodynamic profile evolves due to reduced CAPE and increased CIN.

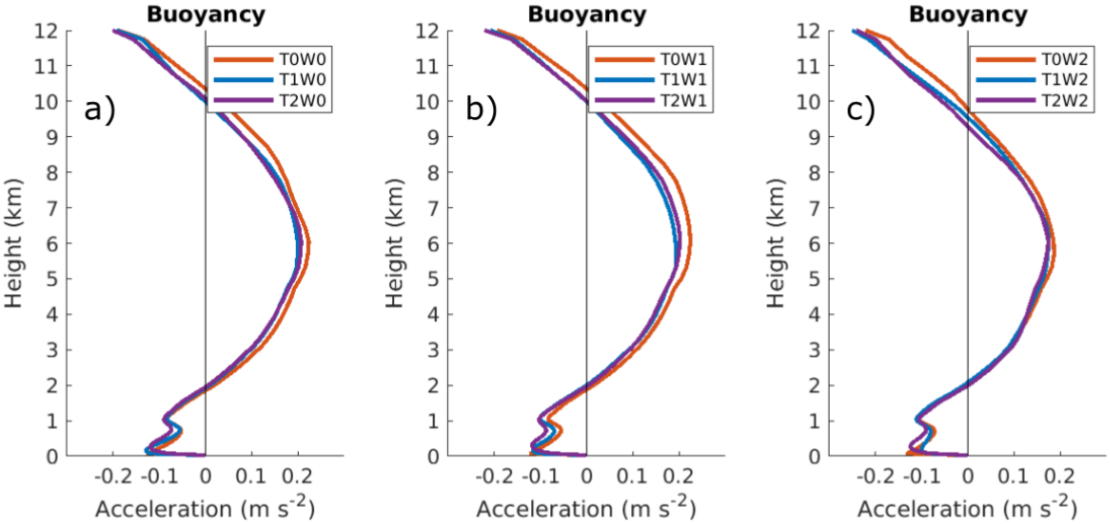

Figure 3.3 Vertical profiles of updraft core buoyancy acceleration grouped by simulations featuring W0 (a), W1 (b), and W2 (c).

In simulations featuring W0 and W1, below 1 km, BUOY becomes more negative as the thermodynamic profile progress through the ET (Figure 3.3a-b). Meanwhile, above 1 km, BUOY is greatest in the simulation featuring T0, and BUOY is similar for the simulations featuring T1 and T2. In the simulations featuring W2, below 1km, BUOY is similar for T0 and T1, and BUOY is most negative for T2 (Figure 3.3c). Above 1 km, BUOY is similar for all three simulations, except BUOY is slightly greater above 5 km.

Overall, BUOY becomes more negative at low levels as the thermodynamic profile progress through the ET, which physically aligns with the increases in CIN through the ET. Meanwhile, BUOY is maximized above 1 km in the pre-transition thermodynamic environment, and BUOY is similar above 1 km in the mid- and post-transition thermodynamic environments. The decreased BUOY in T1 and T2 aligns with decreases in CAPE as the thermodynamic profile progresses through the ET.

3.2.1.2. Kinematic effects on buoyancy acceleration

To investigate the effects of the kinematic evolution during the ET, simulations were grouped by a common thermodynamic profile (Figure 3.4). It is expected that BUOY will be mostly unaffected by kinematic evolution of the ET.

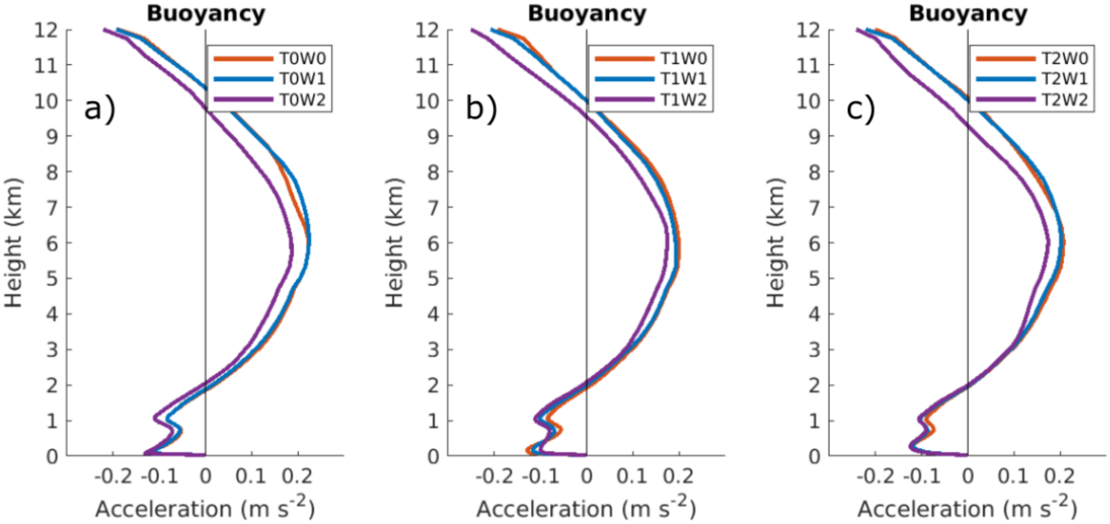

Figure 3.4 Vertical profiles of updraft core buoyancy acceleration grouped by simulations featuring T0 (a), T1 (b), and T2 (c).

For simulations sharing the T0 profile, BUOY is the least throughout the profile for W2. (Figure 3.4a). Meanwhile, BUOY is nearly identical for W0 and W1. For simulations featuring T1, near the surface, BUOY becomes slightly less negative as the ET progresses (Figure 3.4b). Around 1 km BUOY becomes increasing negative through the ET. Above 3 km, BUOY is similar for W0 and W1, while BUOY is the least for W2. Lastly, for simulations featuring T2, BUOY is similar throughout the profile, except BUOY is the least for W2 above 3 km (Figure 3.4c). Overall, for a given thermodynamic profile, BUOY is the least in simulations featuring W2, and BUOY is similar for simulations featuring W0 and W1.

Figure 3.5 shows example plan views of BUOY in relation to the updraft core and radar reflectivity at heights of 100 m (a) and 5163 m (b). Most low-level updraft core points are located along the leading edge of the cold pool, where the horizontal buoyancy gradient is largest (Figure 3.5a).

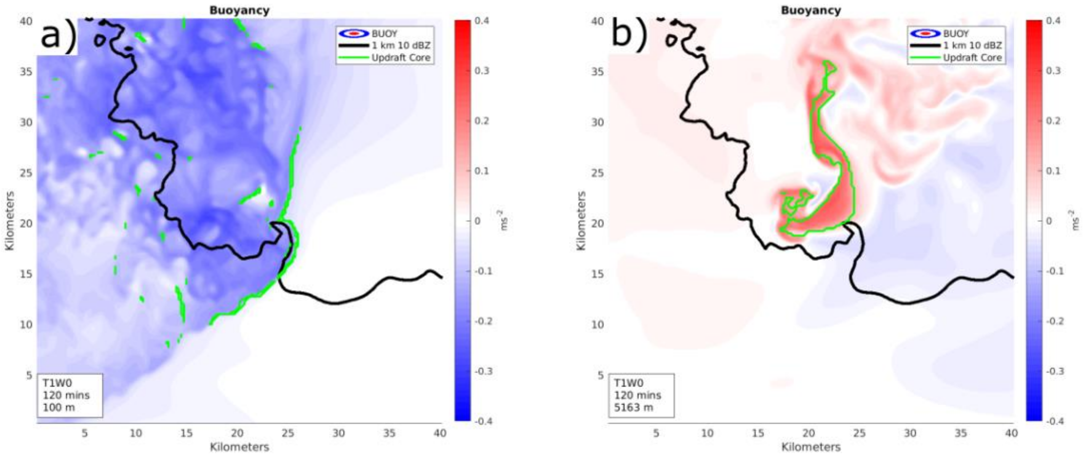

Figure 3.5 Similar to Figure 3.1 but featuring contours of buoyancy acceleration.

3.2.2. Buoyancy pressure acceleration

3.2.2.1. Thermodynamic effects on buoyancy pressure acceleration

To investigate the effects of the thermodynamic evolution during the ET, simulations were grouped by a common kinematic profile (Figure 3.6).

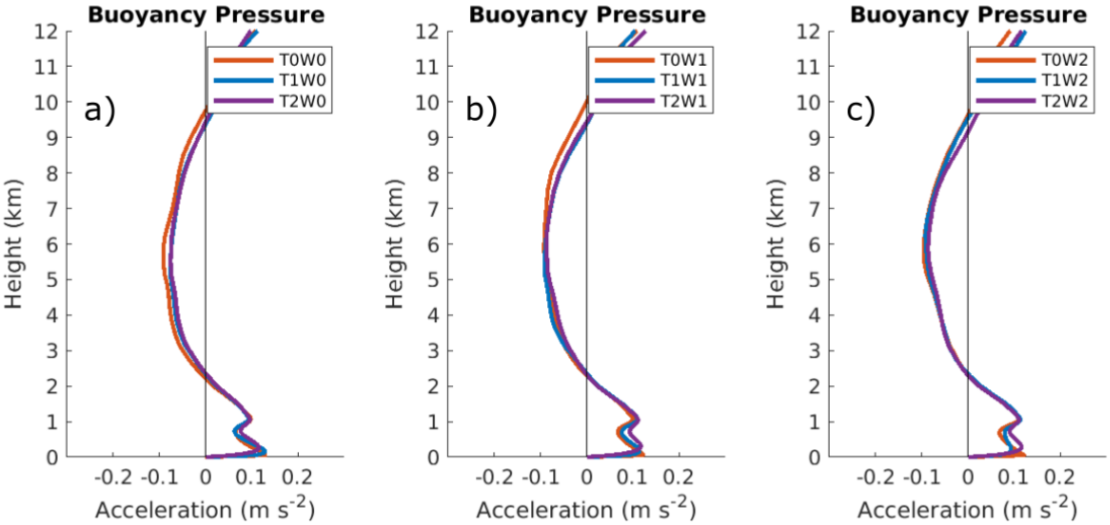

Figure 3.6 Vertical profiles of updraft core buoyancy pressure acceleration grouped by simulations featuring W0 (a), W1 (b), and W2 (c).

In simulations featuring W0, BP in the lowest 1 km is slightly greater for T2 than for T0 and T1 (Figure 3.6a). Meanwhile, above 2 km, BP is the most negative for T0. For simulations featuring W1, BP increases through the ET below 1 km (Figure 3.6b). Above 1 km, BP is similar across all three simulations, except BP is less for T0 above 6 km. In simulations featuring W2, BP in the lowest 1 km increases through the ET (Figure 3.6c). Between 1 km and 8 km, BP is mostly unchanged. Overall, low-level BP increases as the thermodynamic profile progresses through the ET and acts to offset the reduction in low-level BUOY. Above 1 km, BP is generally the most negative in simulations featuring T0 and offsets the greater BUOY in those simulations.

3.2.2.2. Kinematic effects on buoyancy pressure acceleration

To investigate the effects of the kinematic evolution during the ET, simulations were grouped by a common thermodynamic profile (Figure 3.7).

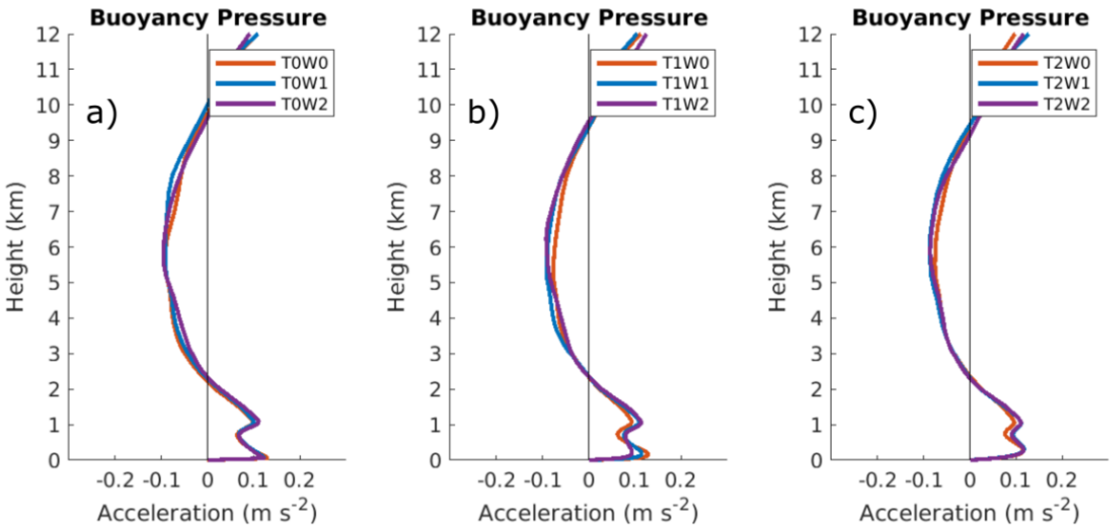

Figure 3.7 Vertical profiles of updraft core buoyancy pressure acceleration grouped by simulations featuring T0 (a), T1 (b), and T2 (c).

In simulations featuring T0, BP is similar for all three wind profiles (Figure 3.7a). For simulations featuring T1, BP near the surface decreases slightly through the ET (Figure 3.7b). Meanwhile, BP is the least in magnitude by small margins for the W0 profile around 1 km and between 5 km and 8 km. In simulations featuring T2, BP is slightly less in magnitude for W0 than for W1 and W2 around 1 km (Figure 3.7c). Otherwise, BP is similar above 2 km. Overall, BP is mostly unaffected changes to the kinematic profile.

Figure 3.8 shows example plan views of BP in relation to the updraft core and radar reflectivity at heights of 100 m (a) and 5163 m (b).

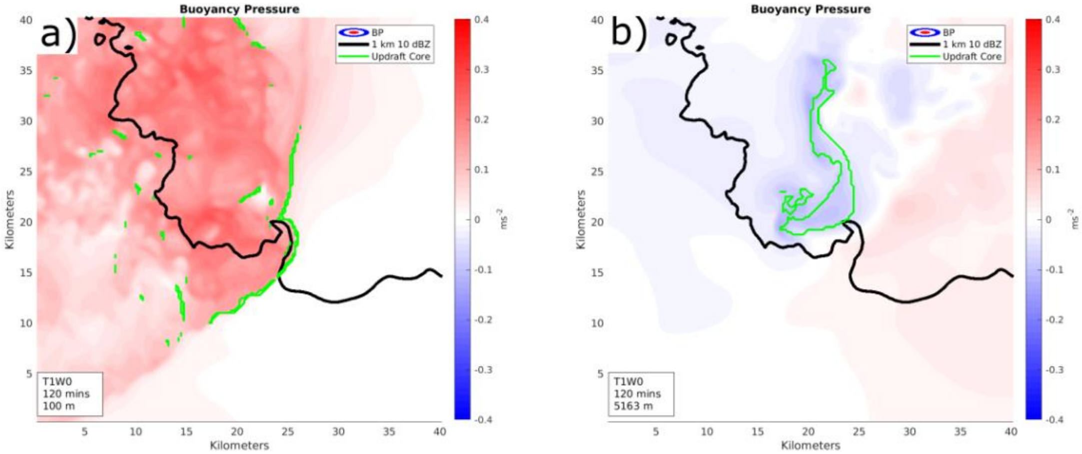

Figure 3.8 Similar to Figure 3.1 but featuring contours of buoyancy pressure acceleration.

3.2.3. Dynamic acceleration

3.2.3.1. Thermodynamic effects on dynamic acceleration

To investigate the effects of the thermodynamic evolution during the ET, simulations were grouped by a common kinematic profile (Figure 3.9). It is expected that DYN will be mostly unaffected by thermodynamic evolution of the ET.

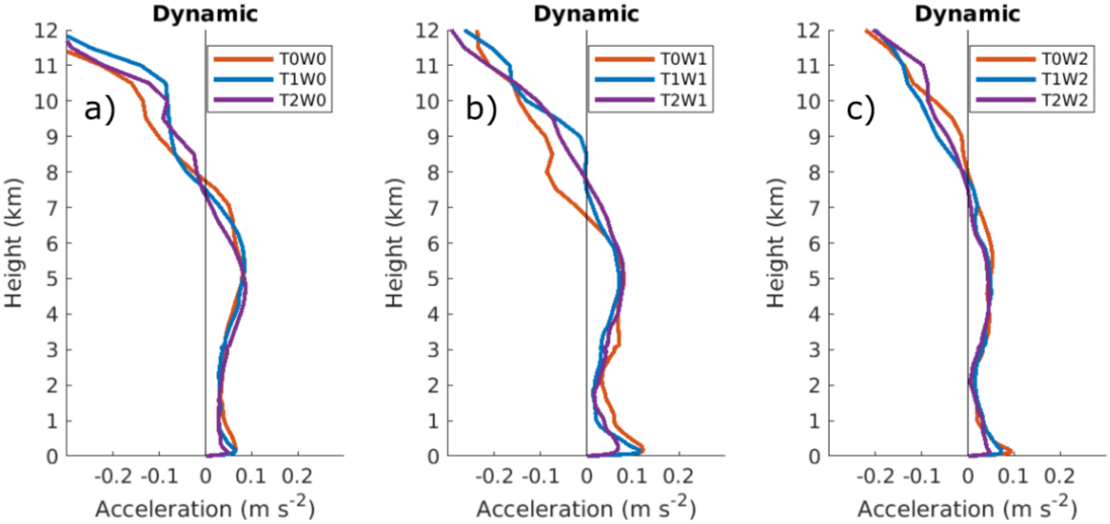

Figure 3.9 Vertical profiles of updraft core dynamic acceleration grouped by simulations featuring W0 (a), W1 (b), and W2 (c).

In simulations featuring W0, DYN near the surface is weakest for T2, while DYN for T0 and T1 is similar (Figure 3.9a). Moving up the profile, DYN for T1 decreases to the same value as T2 by 1 km, and DYN for T0 decreases to the same value as T1 and T2 by 2 km. From 2 km to 5 km, DYN for T2 is slightly larger than DYN for T0 and T1. Between 5 km and 8 km, all three DYN profiles decrease to zero. T2 starts to decrease at the lowest height, and T0 starts to decrease at the greatest height. In simulations featuring W1, DYN near the surface is weakest for T2, while DYN for T0 and T1 is similar (Figure 3.9b). DYN for T1 decreases to the same value as T2 by 1 km and remains similar from 1 km to 8 km. DYN below 4 km is greatest for the T0 profile. For the simulations featuring W2, DYN near the surface decreases as the ET progresses (Figure 3.9c). Between 1 km and 8 km, DYN for all three thermodynamic profiles is mostly similar. Overall, low-level DYN is similar in simulations featuring T0 and T1, and low-level DYN is weaker in T2 simulations. The reduction in DYN later in the ET was unexpected and will be investigated in further detail in section 3.2.3.3.

3.2.3.2. Kinematic effects on dynamic accelerations

To investigate the effects of the kinematic evolution during the ET, simulations were grouped by a common thermodynamic profile (Figure 3.10). It is expected that low-level DYN will increase through the ET as the LLJ strengthens and SRH increases.

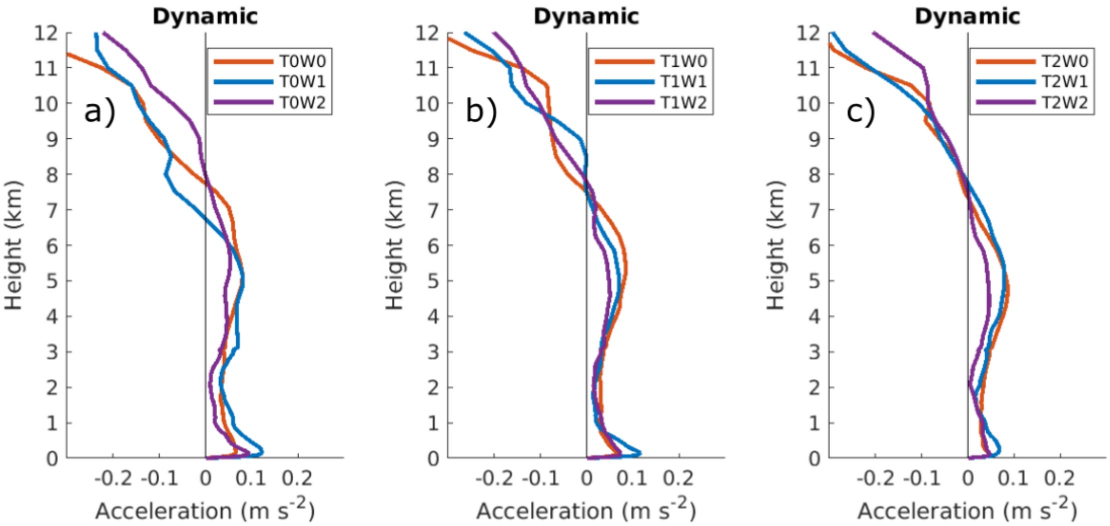

Figure 3.10 Vertical profiles of updraft core dynamic acceleration grouped by simulations featuring T0 (a), T1 (b), and T2 (c).

In simulations featuring T0, DYN is greatest for W1 from the surface to 5 km (Figure 3.10a). Near the surface, DYN is greater for W2 than for W0. Otherwise below 6 km, DYN for W2 is the least. In simulations featuring T1, DYN below 1 km is greatest for W1 and similar for W0 and W2 (Figure 3.10b). Between 1 km and 4 km, all three simulations feature similar DYN. Between 4 km and 8 km, DYN decreases as the ET progresses. For simulations featuring T2, DYN in the lowest 1 km is greatest for W1 and similar for W0 and W2 (Figure 3.10c). Above 1 km, DYN for W0 and W1 is similar, while DYN for W2 is the least. Overall, low-level DYN is greatest for simulations featuring W1, while low-level DYN is similar for simulations featuring W0 and W2. It was expected that low-level DYN would increase as the kinematic profile evolved through the ET. While low-level DYN increased from W0 to W1, the decrease in low-level DYN from W1 to W2 will be explored further in the next section. Additionally, mid-level DYN is generally similar for W0 and W1 but weaker for W2.

Figure 3.11 shows example plan views of DYN in relation to the updraft core and radar reflectivity at heights of 100 m (a) and 5163 m (b).

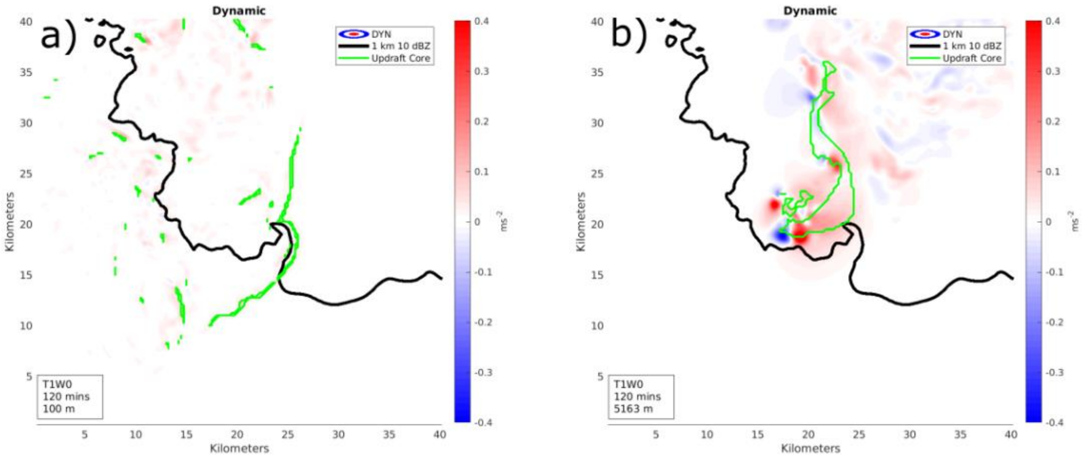

Figure 3.11 Similar to Figure 3.1 but featuring contours of buoyancy pressure acceleration.

3.2.3.3. Physical mechanisms leading to decreased low-level dynamic accelerations late in the ET.

In section 3.2.3.1, low-level DYN was weakest in simulations featuring T2 despite being similar in simulations featuring T0 and T1, and in section 3.2.3.2, low-level DYN was weaker in W2 simulations than in W1 simulations despite W2 featuring a stronger LLJ and greater SRH. Neither of these results were expected and require further analysis. Therefore, the pressure perturbations that contribute to dynamic VPPGF will be broken down into their primary components: “spin” from vorticity and “splat” from deformation. Oftentimes, the dynamic pressure perturbation is formulated in terms of the perturbation wind field. This formulation gives rise to the nonlinear and linear components. However, because the linear acceleration is small compared to the nonlinear acceleration, the two terms have been combined to form DYN. So, the dynamic pressure perturbation can be written in terms of the full wind field. Thus, the linear term is accounted for within the deformation term, and the dynamic pressure perturbation is:

$$p'_d \propto e_{ij}^2 - \tfrac{1}{2}|\vec{\omega}|^2.$$

The deformation term is:

$$e_{ij}^2 = \frac{1}{4}\sum_{i=1}^{3}\sum_{j=1}^{3}\left(\frac{\partial u_i}{\partial x_j} + \frac{\partial u_j}{\partial x_i}\right)^2$$

where $u_1 = u$, $u_2 = v$, $u_3 = w$, $x_1 = x$, $x_2 = y$, and $x_3 = z$. The vorticity term is:

$$-\frac{1}{2}|\vec{\omega}|^2$$

where $\vec{\omega}$ is the three-dimensional vorticity vector (Markowski and Richardson, 2010). The deformation term will always contribute positive pressure perturbations, and the vorticity term will always contribute negative pressure perturbations. The dynamic acceleration term is:

$$\frac{dw}{dt} \sim -\frac{1}{\rho_0}\frac{\partial p'_d}{\partial z}.$$

Thus, dynamic pressure perturbations that decrease with height will result in positive vertical dynamic accelerations.

To investigate the decreased low-level DYN in T2 simulations, first, profiles of updraft core spin are grouped by common kinematic profile (Figure 3.12).

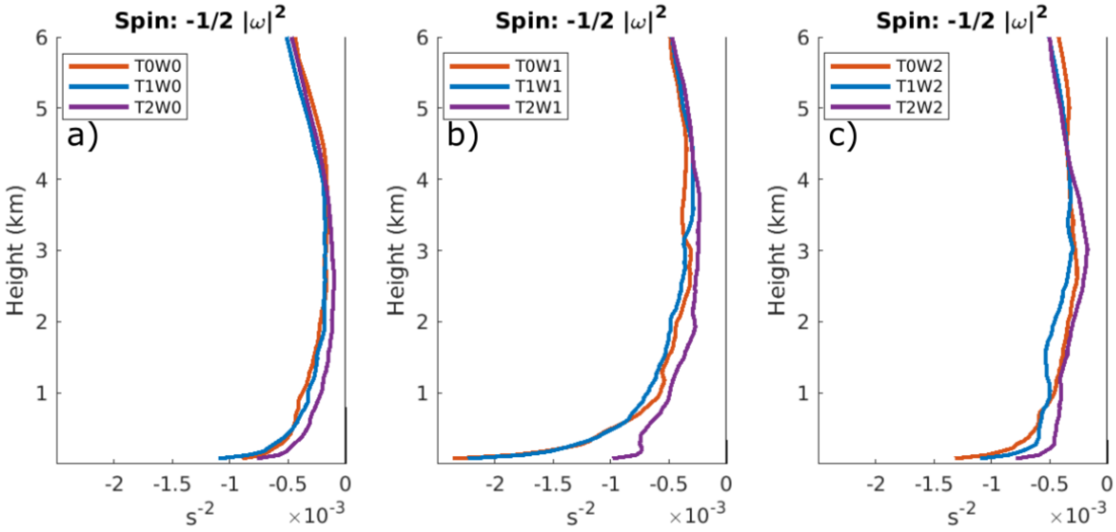

Figure 3.12 Vertical profiles of updraft core spin term grouped by simulations featuring W0 (a), W1 (b), and W2 (c).

Regardless of kinematic profile, the magnitude of the vorticity term in the lowest 4 km is the weakest for simulations featuring the T2 profile (Figure 3.12a-c). Therefore, the negative pressure perturbation associated with vorticity term is weakest in T2 environments. One physical mechanism that may contribute to weaker spin in the lowest 4 km for T2 simulations is decreased buoyancy. By having less low-level buoyancy acceleration in T2 simulations, vertical vorticity within the mesocyclone would experience less amplification from midlevel vorticity stretching. Thus, if midlevel vertical vorticity is weaker, the low-level vertical gradient in vorticity would be weaker, and the vorticity term would decrease. Next, profiles of updraft core splat were grouped by common kinematic profile (Figure 3.13).

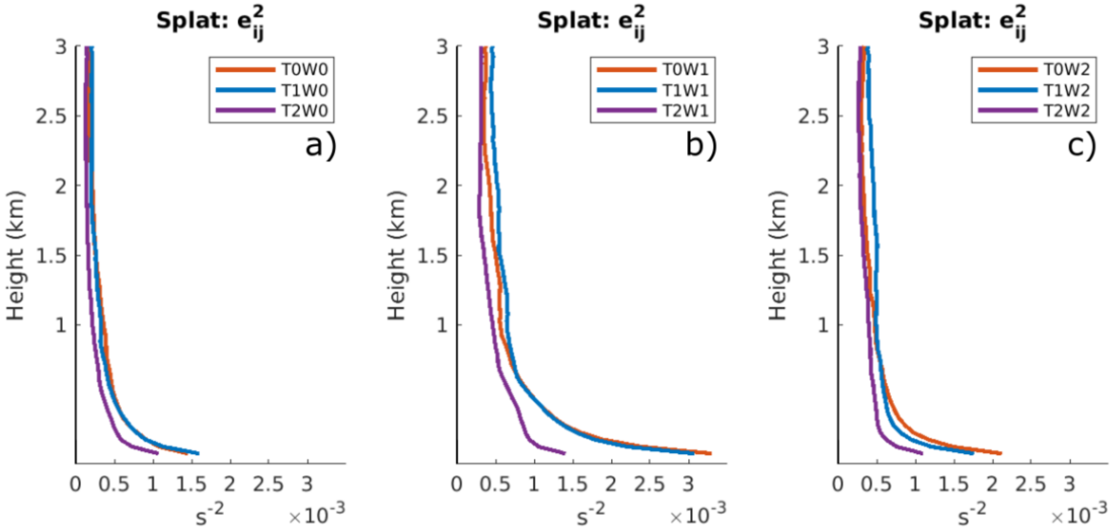

Figure 3.13 Vertical profiles of updraft core splat grouped by simulations featuring W0 (a), W1 (b), and W2 (c).

For all kinematic profiles, the splat term in the lowest 3 km is the weakest for T2 simulations, while the splat term is similar for T0 and T1 simulations (Figure 3.13a-c). Additionally, the difference in splat between T0 and the other thermodynamic profiles is most pronounced near the surface, so the dynamic pressure perturbation contributed by the splat term near the surface is reduced. One mechanism that may impact the near-surface splat of T2 environments is the cooler near-surface base environment. Because the near-surface environment is the coolest in T2, the difference in θ between the cold pool and the environment will be minimized for T2. Thus, the cold pool likely propagates slower, reducing horizontal convergence along the leading edge of the cold pool and, consequently, the deformation term Therefore, T2 simulations feature both reduced positive pressure perturbations near the surface from the deformation term and reduced negative pressure perturbations from spin in the lowest 4 km. Thus, the dynamic VPPGFs in the low levels are weaker in magnitude for T2 simulations than the other simulations. As a result, DYN is also weaker for T2 simulations, because DYN is largely determined by dynamic VPPGFs.

To investigate the weaker low-level DYN in W2 simulations than W1 simulations, first, profiles of updraft core spin are grouped by common thermodynamic profile (Figure 3.14).

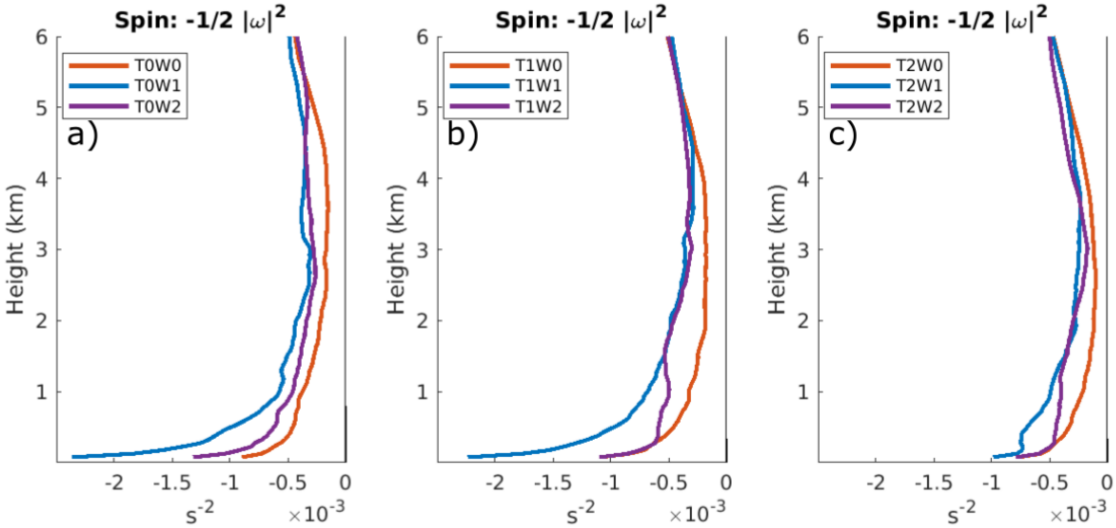

Figure 3.14 Vertical profiles of updraft core spin grouped by simulations featuring T0 (a), T1 (b), and T2 (c).

In the lowest 1 km, across all thermodynamic profiles, the vorticity term is weaker for W2 than for W1. Therefore, the magnitude of negative pressure perturbation created by vorticity for W2 simulations is less than W1 simulations. Next, profiles of updraft core splat were grouped by common kinematic profile (Figure 3.15).

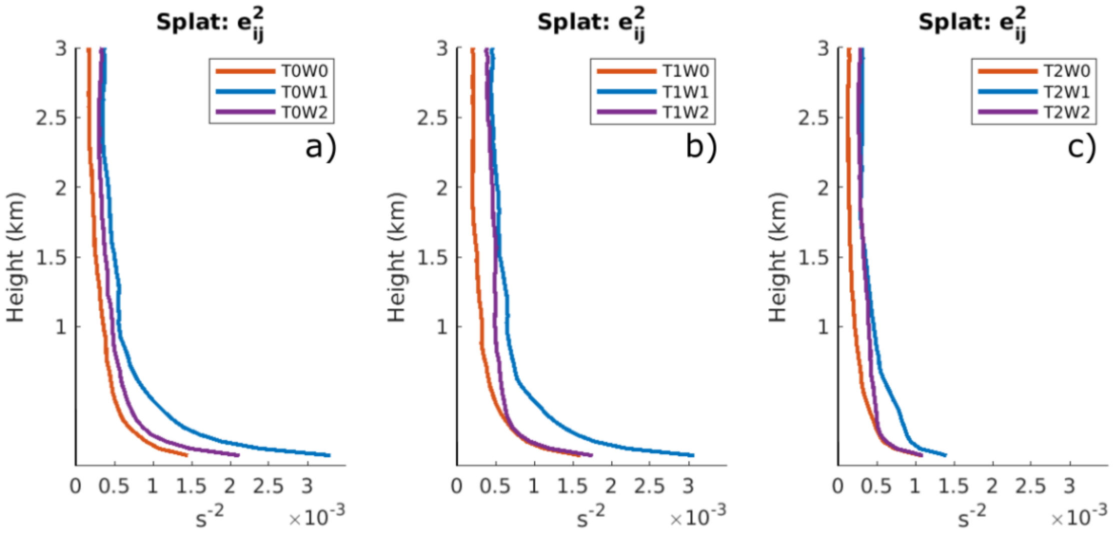

Figure 3.15 Vertical profiles of updraft core splat grouped by simulations featuring T0 (a), T1 (b), and T2 (c).

For all thermodynamic profiles, deformation term in the lowest 1 km for W2 is less than for W1. The greatest difference in the deformation term between W2 and W1 is near the surface. Therefore, the positive dynamic pressure perturbation from the deformation term is most reduced at the surface. In combination with weaker negative dynamic pressure perturbations from vorticity in the lowest 1 km, the reduced near-surface positive dynamic pressure perturbations from deformation lead to weaker dynamic VPPGFs and weaker low-level DYN.

3.2.4. Net acceleration

NET is the sum of BUOY, BP, and DYN and each height level for each simulation.

3.2.4.1. Thermodynamic effects on net acceleration

To investigate the effects of the thermodynamic evolution during the ET, simulations were grouped by a common kinematic profile (Figure 3.16).

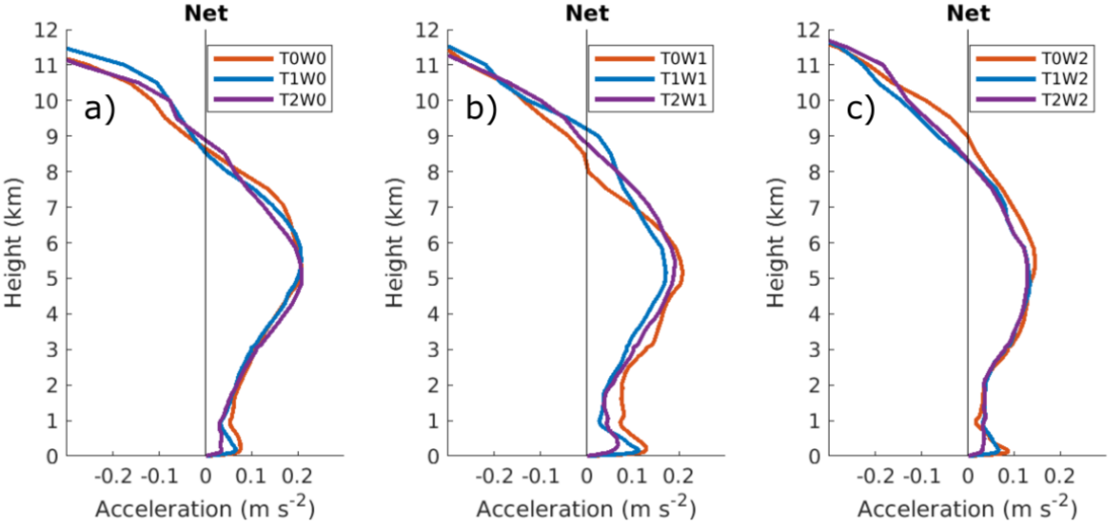

Figure 3.16 Vertical profiles of updraft core net acceleration grouped by simulations featuring W0 (a), W1 (b), and W2 (c).

For simulations featuring W0, NET decreases in the lowest 1 km as the thermodynamic profile progresses through the ET (Figure 3.16a). Between 2 km and 6 km, NET is similar for all three thermodynamic profiles. For simulations featuring W1, NET decreases in the lowest 1 km as the thermodynamic profile progresses through the ET (Figure 3.16b). Between 2 km and 7 km, NET is greatest for T0 and least for W1. In simulations featuring W2, NET is similar for T0 and T1, and NET is weakest for T2 (Figure 3.16c). Above 1 km, NET is similar for all three thermodynamic profiles, except T0 is slightly greater than the others above 5 km. Overall, low-level NET decreases as the thermodynamic profile evolves through the ET.

3.2.4.2. Kinematic effects on net acceleration

To investigate the effects of the kinematic evolution during the ET, simulations were grouped by a common thermodynamic profile (Figure 3.17).

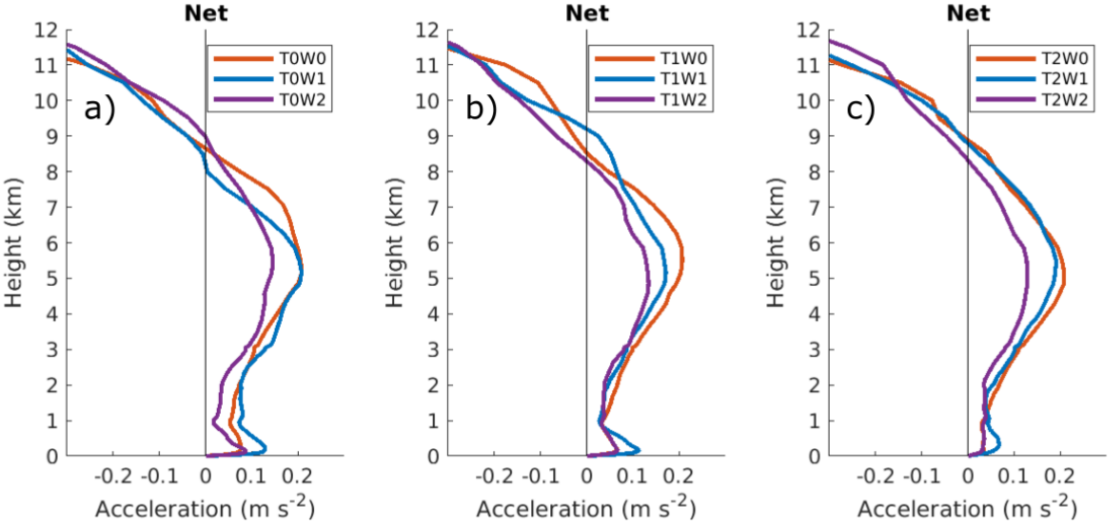

Figure 3.17 Vertical profiles of updraft core net acceleration grouped by simulations featuring T0 (a), T1 (b), and T2 (c).

For simulations featuring T0, NET is greatest for W1 in the lowest 5 km, and NET is the least for W2 in the lowest 7 km (Figure 3.17a). In simulations featuring T1, NET is the greatest in the lowest 1 km for W1 and similar for the others (Figure 3.17b). Between 1 km and 8 km, NET generally decreases as the kinematic profile progresses through the ET. For simulations featuring T2, NET is the greatest in the lowest 1 km for W1 and similar for the others (Figure 3.17c). Above 2 km, NET for W0 is slightly greater than for W1, and NET for W2 is much less than the others. Overall, low-level NET is greatest in W1 simulations and similar in W0 and W2 simulations. Additionally, mid-level NET generally decreases through the ET, and the difference between W2 and W1 is greater than the difference between W1 and W0.

3.2.5. Vertical velocity

All points within the updraft core at each height level are associated with vertical velocity greater than or equal to the updraft core vertical velocity shown in this section.

3.2.5.1. Thermodynamic effects on vertical velocity

To investigate the effects of the thermodynamic evolution during the ET, simulations were grouped by a common kinematic profile (Figure 3.18).

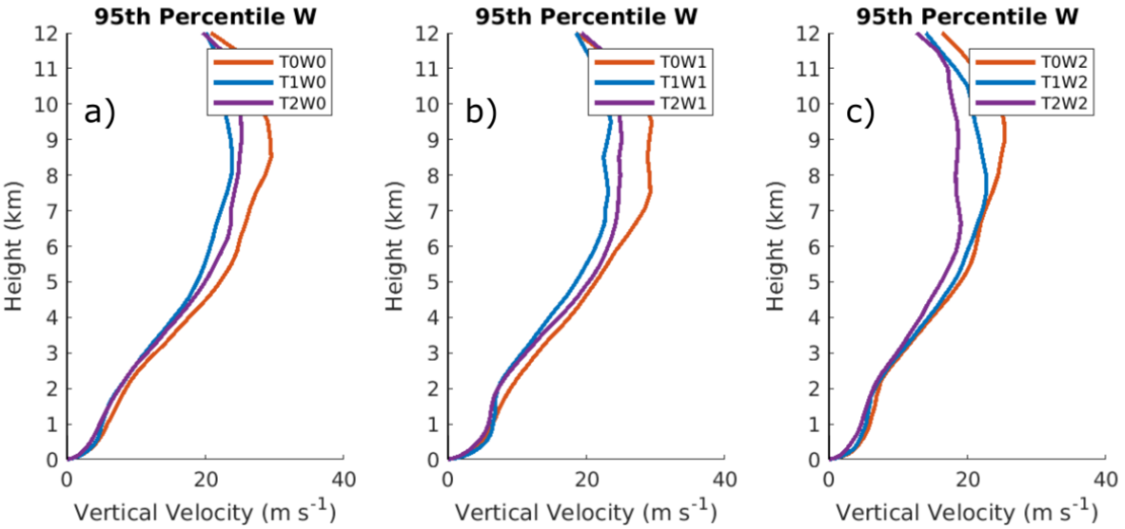

Figure 3.18 Vertical profiles of updraft core threshold vertical velocity grouped by simulations featuring W0 (a), W1 (b), and W2 (c).

For simulations featuring W0 and W1, TW above 1 km is greatest for T0 (Figure 3.18a-b). TW is similar for T1 and T2 below 4 km, above which T2 is greater. In simulations featuring W2, TW is similar for all three thermodynamic profiles below 3km (Figure 3.18c). Above 3 km, TW decreases as the thermodynamic profile progresses through the ET. Overall, TW below 1 km is mostly unaffected by thermodynamic changes during the ET, and TW above 1 km is greatest for the T0 profile. Interestingly, in two of the three cases (Figure 3.18a-b), mid-level TW is greater for the T2 simulation than for the T1 simulation. The difference is likely driven by slightly greater mid-level DYN for T2 simulations (Figure 3.9 a-b).

3.2.5.2. Kinematic effects on vertical velocity

To investigate the effects of the thermodynamic evolution during the ET, simulations were grouped by a common kinematic profile (Figure 3.19).

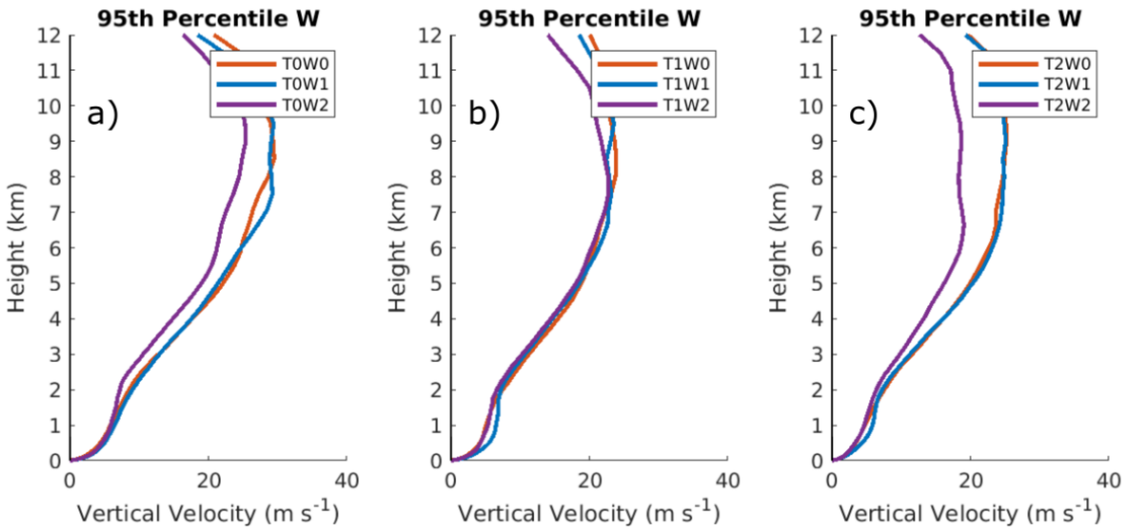

Figure 3.19 Vertical profiles of updraft core threshold vertical velocity grouped by simulations featuring T0 (a), T1 (b), and T2 (c).

For simulations featuring T0, TW below 1 km is similar amongst all kinematic profiles (Figure 3.19a). Above 1 km, TW for W0 and W1 is similar, and TW for W2 is the weakest. For simulations featuring T1, TW in the lowest 2 km is greatest for W1 (Figure 3.19b). Otherwise, TW is similar amongst all the simulations. In simulations featuring T2, TW in the lowest 1 km is greatest for W1 (Figure 3.19c). Above 2 km, TW for W0 and W1 is similar, and TW for W2 is the weakest. Overall, W1 simulations feature the greatest TW below 2 km, and W2 simulations feature the weakest TW above 2 km.

3.3. Effects of environmental changes during the ET on near-surface vertical vorticity stretching.

The stretching of near-surface vertical vorticity can be an important physical mechanism during tornadogenesis (Markowski and Richardson, 2014; Coffer and Parker, 2015). It is expected that the kinematic changes of the ET will be favorable to near-surface vertical vorticity stretching (VVS). To investigate the effects thermodynamic and kinematic changes during the ET may have on near-surface VVS, the vertical vorticity stretching term, $\zeta \frac{\partial w}{\partial z}$, was calculated at each model grid point and will be compared amongst simulations. For each simulation, the time of maximum vertical vorticity within the storm domain and during the mature storm period will be analyzed at a height of 75 m, which is the lowest height level for which every simulation has updraft core points. Thus, any trends in VVS amongst simulations can be related to the updraft acceleration results of previous sections.

Contours of VVS at a height of 75 m within the storm domain for simulations featuring T0 are plotted in Figure 3.20. To compare VVS between simulations, the magnitude and area of regions of positive VVS are of interest. Right-moving supercells are generally associated with cyclonic tornadoes. Thus, positive VVS is favorable for tornadogenesis because it would amplify cyclonic vertical vorticity.

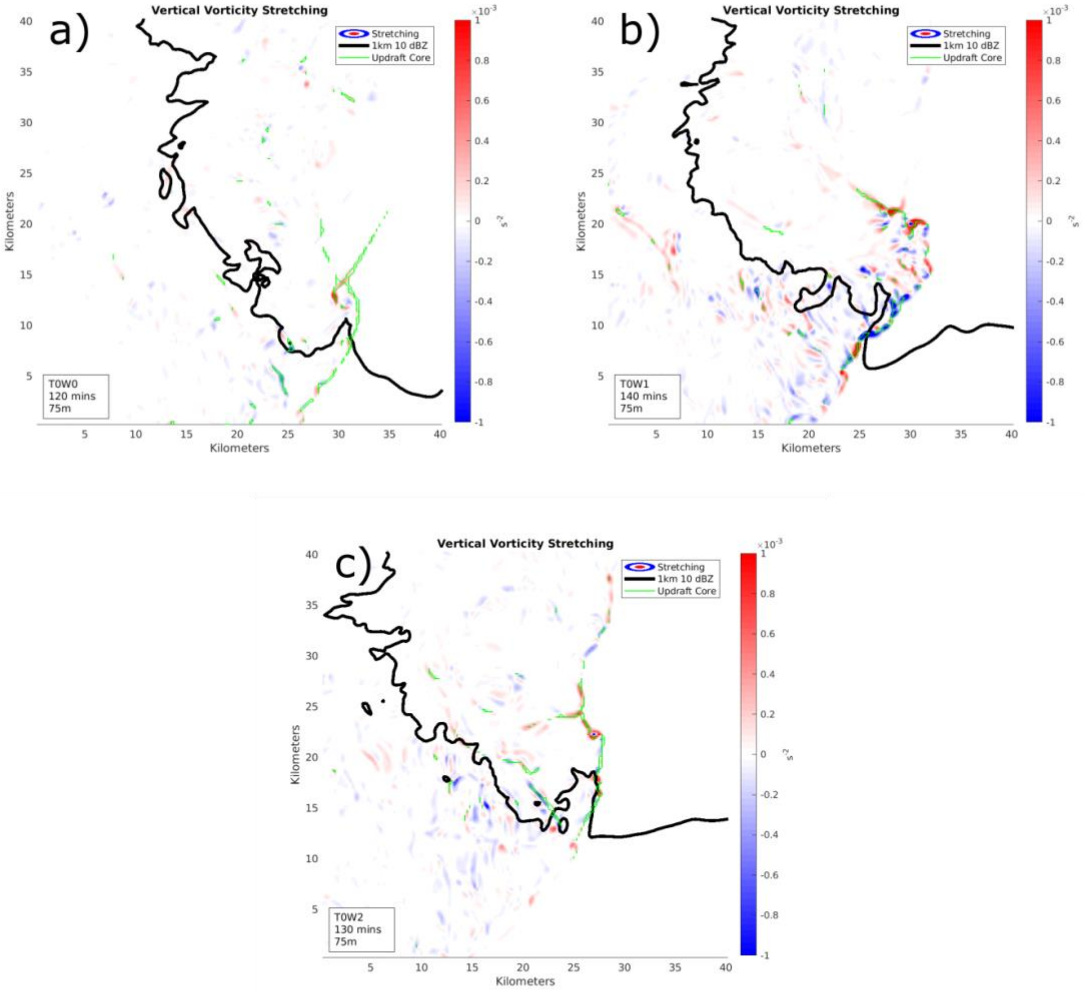

Figure 3.20 Plan view of vertical vorticity stretching contours within the storm domain at a height of 75 m from times of maximum vertical vorticity during the mature storm period of each simulation. The radar reflectivity contour of 10 dBZ is overlaid in black, and the updraft core contour is overlaid in green. Simulations all feature T0 with kinematic profiles W0 (a), W1 (b), and W2 (c).

In Figure 3.20, it appears that the regions of positive VVS are largest and most intense in the T0W1 simulation (b) and are smallest and weakest in the T0W0 simulation (c). However, it is difficult to clearly compare between simulations using plan views. So, using the same temporal and spatial criteria applied in Figure 3.20, histograms featuring the number of grid points with positive VVS greater exceeding 10^{-4} s^{-2} were created for each simulation (Figure 3.21).

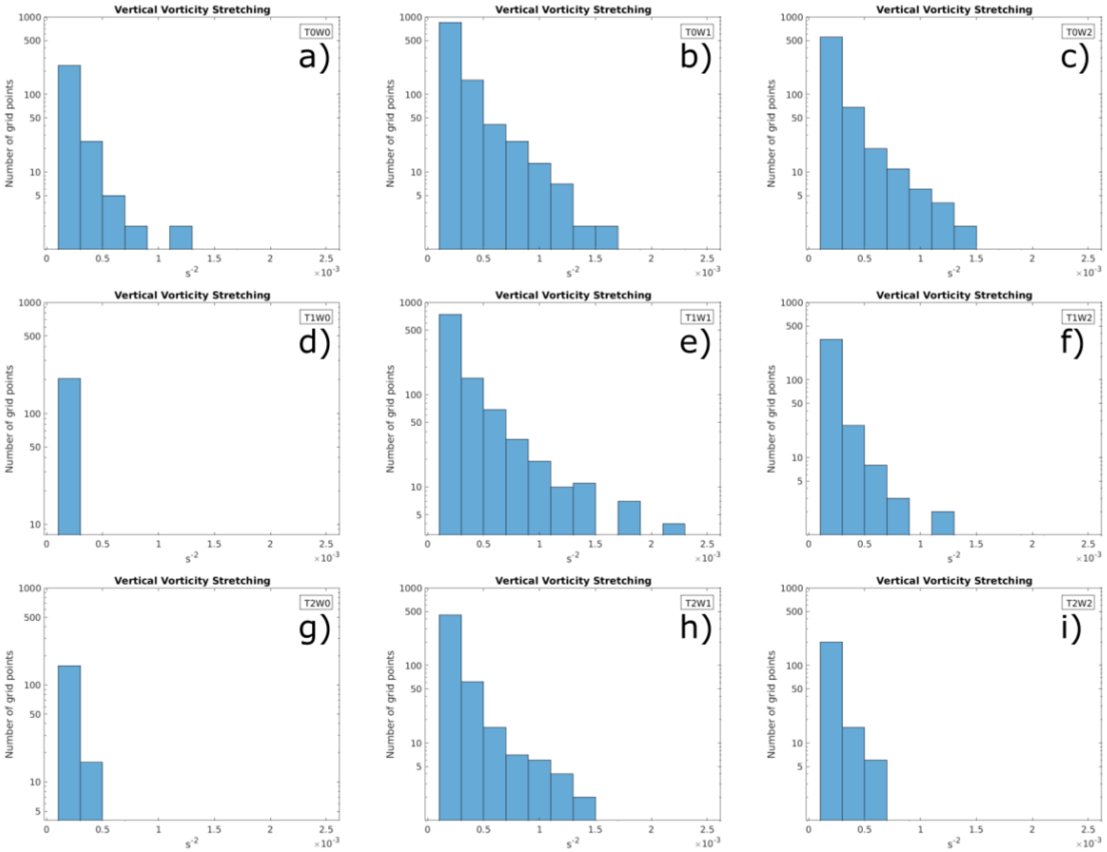

Figure 3.21 Histograms of vertical vorticity stretching exceeding 10^{-4} s^{-2} within the storm domain at a height of 75 m and at the time of maximum vertical vorticity for each simulation. Note that the y-axis of each histogram is logarithmic.

First, the thermodynamic effects on VVS will be investigated. For simulations featuring W0 (Figure 3.21 a, d, and g), as the thermodynamic profile progressed through the ET, the number of grid points exceeding the VVS threshold decreased. Additionally, the greatest VVS values occurred in the T0 simulation, while the maximum VVS in the T1 and T2 simulations were similar. For simulations featuring W1 (Figure 3.21 b, e, and h), as the thermodynamic profile progressed through the ET, the number of grid points exceeding the VVS threshold decreased. Additionally, the greatest VVS values occurred in the T1 simulation, while the maximum VVS in the T0 and T2 simulations were similar. For simulations featuring W2 (Figure 3.21 c, f, and i), as the thermodynamic profile progressed through the ET, the number of grid points exceeding the VVS threshold and the maximum VVS value decreased. Overall, the area of positive VVS decreases as the thermodynamic profile evolves through the ET, and the early periods of the ET are more favorable to strong VVS. These VVS trends physically align with decreasing low-level NET as the thermodynamic profile progresses through the ET.

Next, the kinematic effects on VVS will be investigated. For each grouping of simulations by common thermodynamic profile, T0 (Figure 3.21 a, b, and c), T1 (Figure 3.21 d, e, and f), and T2 (Figure 3.21 g, h, and i), positive VVS exceeding the threshold in the simulations featuring W1 is the strongest and most widespread. W1 also features the strongest low-level NET due to strong low-level DYN. Meanwhile, positive VVS was consistently the weakest and least frequent in simulations featuring W0. Despite similar low-level NET between W0 and W2 simulations, W2 simulations are more favorable for VVS, likely due to greater SRH.

4. CONCLUSIONS

This study investigated the effects of low-level thermodynamic and kinematic changes characteristic of the ET on supercell updraft accelerations. The first hypothesis expected low-level vertical velocity and the relative contribution of low-level dynamic accelerations to increase through the ET while both the thermodynamic and kinematic profiles varied amongst the chosen simulations. It also expected mid-level and peak updraft velocity to decrease through the ET. The first hypothesis was tested in section 3.1. The primary takeaway points of that section are that the relative contributions of dynamic accelerations increase at low height levels only during the early stages of the ET, and mid-level and peak updraft speed decrease through the ET.

The second hypothesis of the study expected the thermodynamic evolution of the ET would lead to decreased buoyancy accelerations and the kinematic evolution of the ET would lead to increased dynamic accelerations, particularly at low height levels. The second hypothesis was tested in section 3.2 and focused on isolating the effects of either the thermodynamic or kinematic evolution of the ET on each updraft acceleration term.

The effects of the thermodynamic evolution during the ET will be summarized first. BUOY becomes more negative at low levels as the thermodynamic profile progress through the ET. Meanwhile, BUOY is maximized above 1 km in the T0 environment and is similar above 1 km in the T1 and T2 environments. BP at low levels increases as the thermodynamic profile progresses through the ET. Above 1 km, BP is slightly more negative in simulations featuring T0 than simulations featuring T1 and T2. DYN at low levels is similar in simulations featuring T0 and T1 but weaker in T2 simulations. NET at low levels decreases as the thermodynamic profile evolves through the ET. TW below 1 km is mostly unaffected by thermodynamic changes during the ET, and TW above 1 km is greatest for the T0 profile.

Next, the effects of the kinematic evolution during the ET will be summarized. BUOY is the least in simulations featuring W2, and BUOY is similar for simulations featuring W0 and W1. BP is mostly unaffected by changes to the kinematic profile. DYN at low levels is greatest for simulations featuring W1 and is similar for simulations featuring W0 and W2. DYN at mid-levels is generally similar for W0 and W1 but weaker for W2. NET at low levels is greatest in W1 simulations and similar in W0 and W2 simulations. NET at mid-levels generally decreases through the ET, and the difference between W2 and W1 is greater than the difference between W1 and W0. W1 simulations feature the greatest TW below 2 km, and W2 simulations feature the weakest TW above 2 km.

The final hypothesis of this study expected near-surface vertical vorticity stretching to increase as the kinematic profile progressed through the ET. The third hypothesis was tested in section 3.3 and focused on the quantity of grid points with positive VVS and the magnitude of VVS. The thermodynamic progression of the ET is unfavorable to VVS. The W1 and W2 profiles are substantially more favorable for VVS than W0, and W1 is more favorable than W2.

The takeaway point from this work most applicable to operational forecasting likely is the introduction and development of the LLJ early in the ET amplifies both dynamic accelerations and vertical vorticity stretching at low levels. Thus, accurate prediction and detection of LLJ onset likely is important to accurately forecast the production of tornadoes by supercell thunderstorms during the early ET. Another interesting takeaway point is that a stronger LLJ with more SRH isn't necessarily more favorable for low-level dynamic accelerations. Also, it is interesting that as the thermodynamic profile evolves through the ET, low-level buoyancy pressure accelerations increase to largely offset the decrease in low-level buoyancy accelerations.

An important caveat of this work is the storm in each simulation was initialized and evolved in a time-invariant base state environment. However, in nature, storms that occur during the ET would be initiated in an environment that is evolving with time. Therefore, future work should simulate supercells during the ET in environments that evolve in time within the simulation by using a technique such as base state substitution or by applying radiation physics and surface fluxes within the simulation. The relationship between supercells and the characteristics of the ET should also be studied across a wider range of possible environments. For example, the LLJ profiles used in this study were developed from LLJ climatology studies and represent only one likely LLJ evolution. Future studies should study the impacts of a wider range of LLJ characteristics such as: magnitude, depth, nose height, and direction. Studying a wider range of LLJs would also likely be useful offer more insight into the weakening of dynamic accelerations late in the ET within this study. Another physical aspect of this study that could be investigated in further detail is the moistening of the near-surface atmosphere during the ET. The moistening is dependent upon evapotranspiration which varies with soil moisture and vegetation. There exists a range of possible q_v profile evolutions that may affect buoyancy accelerations, and this study one represents one possible q_v profile evolution.

The most prominent unresolved question that arose from this study is: Why are buoyancy accelerations weaker for W2 environments than W0 and W1 environments? Based on the results of Peters et al. (2019), which correlate storm-relative flow to buoyancy, one possible avenue to explore is differences in storm-relative flow and updraft width between W2 and other simulations.

REFERENCES

Ashley, W. S., A. J. Krmenec, and R. Schwantes, 2008: Vulnerability due to Nocturnal Tornadoes. *Weather and Forecasting*, **23,** 795-807.

Blumberg, W. G., D. D. Turner, S. M. Cavallo, J. D. Gao, J. Basara, and A. Shapiro, 2019: An Analysis of the Processes Affecting Rapid Near-Surface Water Vapor Increases during the Afternoon to Evening Transition in Oklahoma. *Journal of Applied Meteorology and Climatology*, **58,** 2217-2234.

Bremenkamp, M., and C. J. Nowotarski, 2020: Influences of Anvil Shading on the Evolution of the Supercell Environment and Updraft Accelerations during the Nocturnal Transition. Poster presented at: *Severe Local Storms Symposium*. Boston, MA., Amer. Meteor. Soc., 941.

Bryan, G. H., and J. M. Fritsch, 2002: A benchmark simulation for moist nonhydrostatic numerical models. *Monthly Weather Review*, **130,** 2917-2928.

Coffer, B. E., and M. D. Parker, 2015: Impacts of Increasing Low-Level Shear on Supercells during the Early Evening Transition. *Monthly Weather Review*, **143,** 1945-1969.

Durran, D. R., and J. B. Klemp, 1983: A Compressible Model for the Simulation of Moist Mountain Waves. *Monthly Weather Review*, **111,** 2341-2361.

Gropp, M. E., and C. E. Davenport, 2018: The Impact of the Nocturnal Transition on the Lifetime and Evolution of Supercell Thunderstorms in the Great Plains. *Weather and Forecasting*, **33,** 1045-1061.

Lehmiller, G. S., H. B. Bluestein, P. J. Neiman, F. M. Ralph, and W. F. Feltz, 2001: Wind structure in a supercell thunderstorm as measured by a UHF wind profiler. *Monthly Weather Review*, **129,** 1968-1986.

Markowski, P., and Y. Richardson, 2010: *Mesoscale Meteorology in Madlatitudes.* Wiley-Blackwell, 407 pp.

Markowski, P. M., and Y. P. Richardson, 2014: The Influence of Environmental Low-Level Shear and Cold Pools on Tornadogenesis: Insights from Idealized Simulations. *Journal of the Atmospheric Sciences*, **71,** 243-275.

Morrison, H., G. Thompson, and V. Tatarskii, 2009: Impact of Cloud Microphysics on the Development of Trailing Stratiform Precipitation in a Simulated Squall Line: Comparison of One- and Two-Moment Schemes. *Monthly Weather Review*, **137,** 991-1007.

Naylor, J., and M. S. Gilmore, 2012: Convective Initiation in an Idealized Cloud Model Using an Updraft Nudging Technique. *Monthly Weather Review*, **140,** 3699-3705.

Nowotarski, C. J., P. M. Markowski, and Y. P. Richardson, 2011: The Characteristics of Numerically Simulated Supercell Storms Situated over Statically Stable Boundary Layers. *Monthly Weather Review*, **139,** 3139-3162.

Peters, J. M., C. J. Nowotarski, and H. Morrison, 2019: The Role of Vertical Wind Shear in Modulating Maximum Supercell Updraft Velocities. *Journal of the Atmospheric Sciences*, **76,** 3169-3189.

Shapiro, A., E. Fedorovich, and S. Rahimi, 2016: A Unified Theory for the Great Plains Nocturnal Low-Level Jet. *Journal of the Atmospheric Sciences*, **73,** 3037-3057.

Smith, B. T., R. L. Thompson, J. S. Grams, C. Broyles, and H. E. Brooks, 2012: Convective Modes for Significant Severe Thunderstorms in the Contiguous United States. Part I: Storm Classification and Climatology. *Weather and Forecasting*, **27,** 1114-1135.

Smith, E. N., J. G. Gebauer, P. M. Klein, E. Fedorovich, and J. A. Gibbs, 2019: The Great Plains Low-Level Jet during PECAN: Observed and Simulated Characteristics. *Monthly Weather Review*, **147,** 1845-1869.

Song, J., K. Liao, R. L. Coulter, and B. M. Lesht, 2005: Climatology of the low-level jet at the southern Great Plains atmospheric Boundary Layer Experiments site. *Journal of Applied Meteorology*, **44,** 1593-1606.

Stull, R. B., 1988: *An Introduction to Boundary Layer Meteorology*. Kluwer, 666 pp.

Weisman, M. L., and J. B. Klemp, 1982: The Dependence of Numerically Simulated Convective Storms on Vertical Wind Shear and Buoyancy. *Monthly Weather Review*, **110,** 504-520.

Whiteman, C. D., X. D. Bian, and S. Y. Zhong, 1997: Low-level jet climatology from enhanced rawinsonde observations at a site in the southern Great Plains. *Journal of Applied Meteorology*, **36,** 1363-1376.

APPENDIX A

SUPPLEMENTAL FIGURES

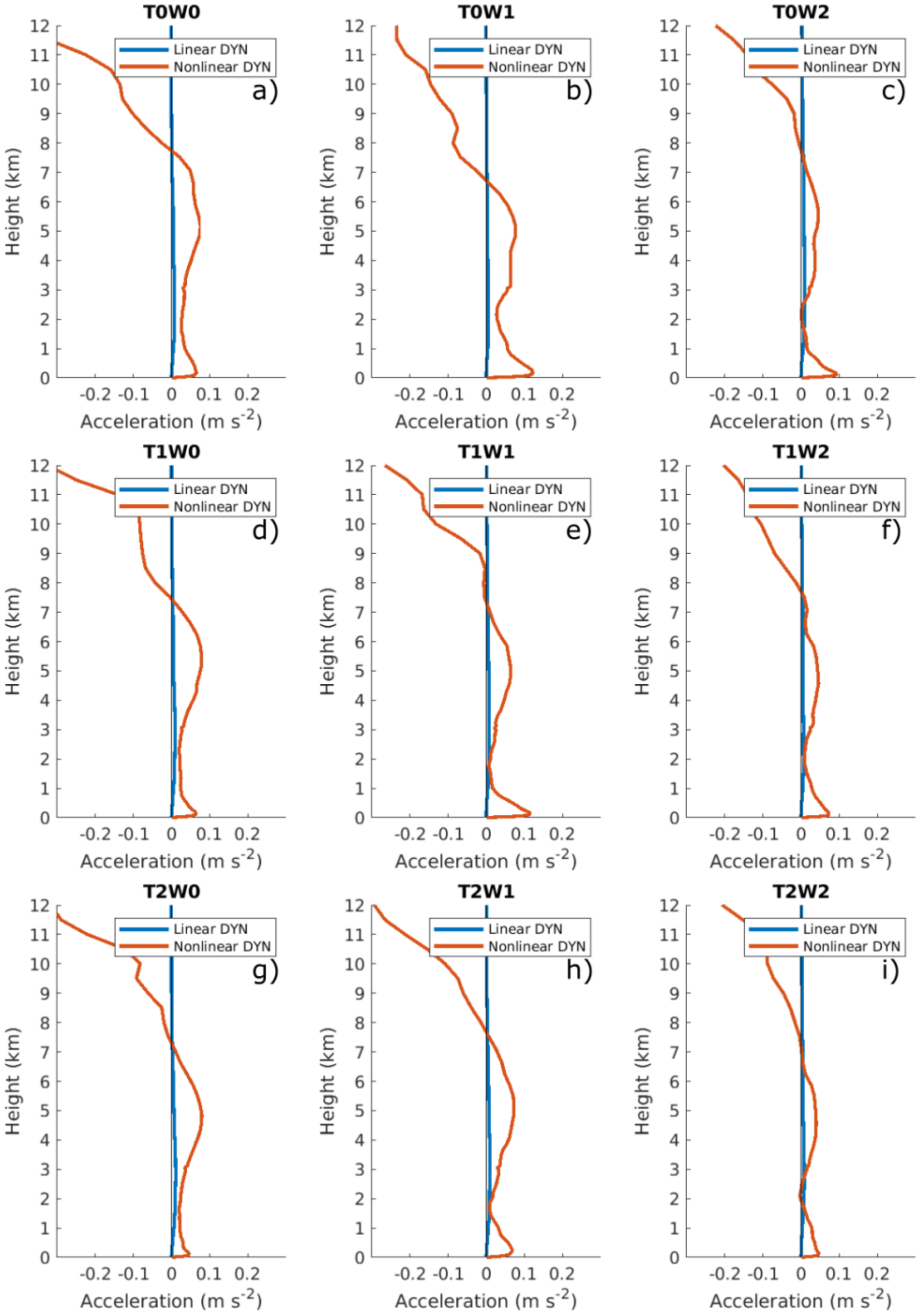

Figure A.1 Vertical profiles of updraft core linear dynamic acceleration (blue) and nonlinear dynamic acceleration (red).